Optimization of Two-Stage Combined Thermoelectric Devices by a Three-Dimensional Multi-Physics Model and Multi-Objective Genetic Algorithm

Jing-Hui Meng [1,2], Hao-Chi Wu [1,3,†] and Tian-Hu Wang [1,2,*]

[1] State Key Laboratory of Alternate Electrical Power System with Renewable Energy Sources, North China Electric Power University, Beijing 102206, China

[2] Research Center of Engineering Thermophysics, North China Electric Power University, Beijing 102206, China

[3] School of Control and Computer Engineering, North China Electric Power University, Beijing 102206, China

* Correspondence: thwang@ncepu.edu.cn; Tel.: +86-10-6177-2783

† Co-first author: due to his equal contribution with the first author.

check for updates

Abstract: Due to their advantages of self-powered capability and compact size, combined thermoelectric devices, in which a thermoelectric cooler module is driven by a thermoelectric generator module, have become promising candidates for cooling applications in extreme conditions or environments where the room is confined and the power supply is sacrificed. When the device is designed as two-stage configuration for larger temperature difference, the design degree is larger than that of a single-stage counterpart. The element number allocation to each stage in the system has a significant influence on the device performance. However, this issue has not been well-solved in previous studies. This work proposes a three-dimensional multi-physics model coupled with multi-objective genetic algorithm to optimize the optimal element number allocation with the coefficient of performance and cooling capacity simultaneously as multi-objective functions. This method increases the accuracy of performance prediction compared with the previously reported examples studied by the thermal resistance model. The results show that the performance of the optimized device is remarkably enhanced, where the cooling capacity is increased by 23.3% and the coefficient of performance increased by 122.0% compared with the 1# Initial Solution. The mechanism behind this enhanced performance is analyzed. The results in this paper should be beneficial for engineers and scientists seeking to design a combined thermoelectric device with optimal performance under the constraint of total element number.

Keywords: thermoelectric generator; thermoelectric cooler; combined thermoelectric device; multi-objective optimization; numerical simulation

1. Introduction

Due to their compact size, light weight, good reliability, cut-price operation, and environmentally friendly operation, thermoelectric devices have attracted great attention in the last several decades [1,2]. Their extensive applications include cooling of electronic chips [3], temperature control [2], heat pump engines [4,5], waste heat recovery to generate electric power [6,7], etc. Thermoelectric devices comprise a thermoelectric generator (TEG) and thermoelectric cooler (TEC). The TEG module connected with an external heat load generates an electrical current through the Seebeck effect [4,8], while the TEC module driven by a power supply pumps heat from the cold end to the hot end by the Peltier effect [1,9]. The phenomena of the Thomson effect, Joule heating effect, Fourier heat conduction effect, and electric conduction effect are always multi-physically coupled either in the TEG or TEC. Generally, for most

practical applications, thermoelectric devices usually operate in single TEG module or single TEC module mode. Focusing on TEC modules, their performance is not only relevant to figure of merit (*ZT*) of the semiconductor materials but also sensitive to the geometric parameters [10–16]. In the past several years, many works have been investigated to improve the performance metrics, and these efforts have made significant progress as well as extended the application of these devices in many fields [17–23].

However, under specific extreme conditions where the environments are too severe, too sensitive, or too confined for conventional heating or cooling techniques, such as aerospace [24–26], isolated mountains or desert areas [27,28], and other geothermal energy exploitation fields [29], there is always the problem of confined space and lack of electricity supply. Thus, a power supply system with a high degree of integration and compact size is required. Harvesting energy from the environment autonomously is one of the smartest solutions to this problem. In addition, with the development of renewable and sustainable energy sources, although the electric grid may not be available in remote areas, solar energy or waste heat are abundant [19,20]. Hence, cooling directly driven by solar power or waste heat source is an appropriate method for many applications. Last but not least, in many energy conversion and management systems, generation of a huge amount of heat which must be removed in time to keep components cool and operational is inevitable [5,6,21]. If the waste heat could be directly used to generate electricity and drive the thermoelectric cooler for cooling, it would not only increase the energy conversion efficiency but also simplify the complexity of the cooling system. Consequently, heat-driven and self-cooling compact thermoelectric devices are required. Recently, combined thermoelectric devices (CTEs), in which a TEC module is driven by a TEG counterpart, have attracted considerable attention due to their advantages of directly converting heat to cooling capacity, integrating the waste heat recovery and compact cooling requirements together, and with no requirement for an associated power source [11,30,31]. Among these combined systems, CTEs with two-stage configurations are an especially promising structure design because they can obtain a much lower cooling temperature [32]. Thus, a CTE with two-stage configuration is considered in the present study.

The literature has evidenced that material properties and structure geometry are significant factors that influence the device performance. Thus, modeling and simulation is a cost-effective way for engineers and scientists to understand, develop, optimize, and control two-stage CTE designs. In the past several years, considerable progress has been made on the underlying mechanisms of the device operation to improve their performance [11,30–42]. These achievements can be classified into numerical modeling, structure design, and optimization methods. For convenience of analysis and comparison, they are summarized in Table 1. In the structure design parameters, the element number for each stage of the two-stage CTE module is a critical issue that influences the performance. This was justified in [11,31]. In the practical design of a CTE system, besides materials and geometric size, the number of elements for each stage is significant for the device performance under the constraint of constant total thermocouple number. This is the determining factor influencing the cooling performance and energy conversion efficiency. However, very little investigation has been performed on the element number allocation design of CTEs.

Besides, the following conclusions about the two-stage structure design can also be reached: (1) most of the models employed are based on thermal resistance model, in which the Thomson effect and temperature-electric potential coupling effect are neglected, leading to the fact they cannot predict the device performance accurately. Thus, a comprehensive multi-physics model is required; (2) although many works examining parameter sensitivity are presented, the focus is mainly on single parameter analysis, however, the factors influencing the device performance are coupled with each other, and the optimal value of a certain specific variable is dependent on the value of other variables. This means that simultaneous optimization of multiple parameters is necessary; (3) the performance metrics to evaluate a CTE include coefficient of performance (COP) and cooling capacity, which are two conflicting objectives. In general, these two indicators cannot reach their maximum values

simultaneously, meaning that obtaining a higher cooling capacity is always on the cost of a deteriorated COP. To solve this contradiction, multi-objective optimization is also necessary.

Based on the above analysis, the motivation of this study lies in optimizing the two-stage CTE by three-dimensional multi-physics model coupled with a multi-objective genetic algorithm to improve its performance. In particular, optimization of element number allocation to each stage of CTE is the main focus, where both the cooling capacity and COP metrics are considered as objective functions.

Table 1. Summary of previous literature *.

Year	Reference	Model	Structure Design	Optimization Method
2006	[30]	TRM	S-CTE	SPA
2006	[31]	TRM	S-CTE	SPA
2009	[32]	TRM	T-CTE	SPA
2010	[33]	TRM	S-CTE	SPA
2010	[34]	TRM	S-CTE	SPA
2012	[35]	TRM	S-CTE	SPA
2012	[36]	TRM	S-CTE	SPA
2014	[11]	Multi-physics Model	S-CTE	SPA
2016	[37]	TRM	S-CTE	SPA
2018	[38]	TRM	S-CTE	Multi-parameter Optimization
2018	[39]	Multi-physics Model	T-CTE	SPA
2018	[40]	Experiment	S-CTE	SPA
2018	[41]	TRM	S-CTE	Multi-parameter Optimization
2018	[42]	TRM	S-CTE	SPA

* In Table 1, "TRM" denotes "Thermal Resistance Model"; "S-CTE" denotes "Single-stage CTE"; "T-CTE" denotes "Two-stage CTE"; "SPA" denotes "Single Parameter Analysis and there is no optimization".

2. Numerical Model

2.1. Structure Design

Figure 1a illustrates the schematic diagram of the studied two-stage CTE device, where the left module is the TEG and the right module is the TEC. Either the TEG or the TEC features two-stages. In the device, Q_{H-G} is absorbed from the hot end of the TEG module, and Q_{L-G} is rejected out of the cold end of the TEG module. This procedure generates an electric current through the Seebeck effect. The generated current is then directly injected into the TEC module, in which Q_{L-C} is absorbed from the cooling object at the cold end and Q_{H-C} is dissipated to the hot end. This procedure is driven by the Peltier effect. All of the element thermocouples in the CTE device are connected in series and thus a single current I flows through each element. The element numbers in the top and the lower stage of the TEG are defined as m_1 and m_2, respectively; the element numbers in the top and the lower stage of the TEC are defined as n_1 and n_2, respectively; m_1, m_2, n_1, and n_2 are the four search variables in the following optimization procedure. The total element number of this combined system is fixed at 40 (i.e., $m_1 + m_2 + n_1 + n_2 = 40$).

The structure of the thermoelectric element as a periodic unit in the combined device is shown in Figure 1b. Each element comprises a P-type and an N-type semiconductor leg, two electrically insulated ceramic plates and three metallic connectors. Each element maintains the same geometric structure in the combined device, and the geometric parameter values are shown in Table 2.
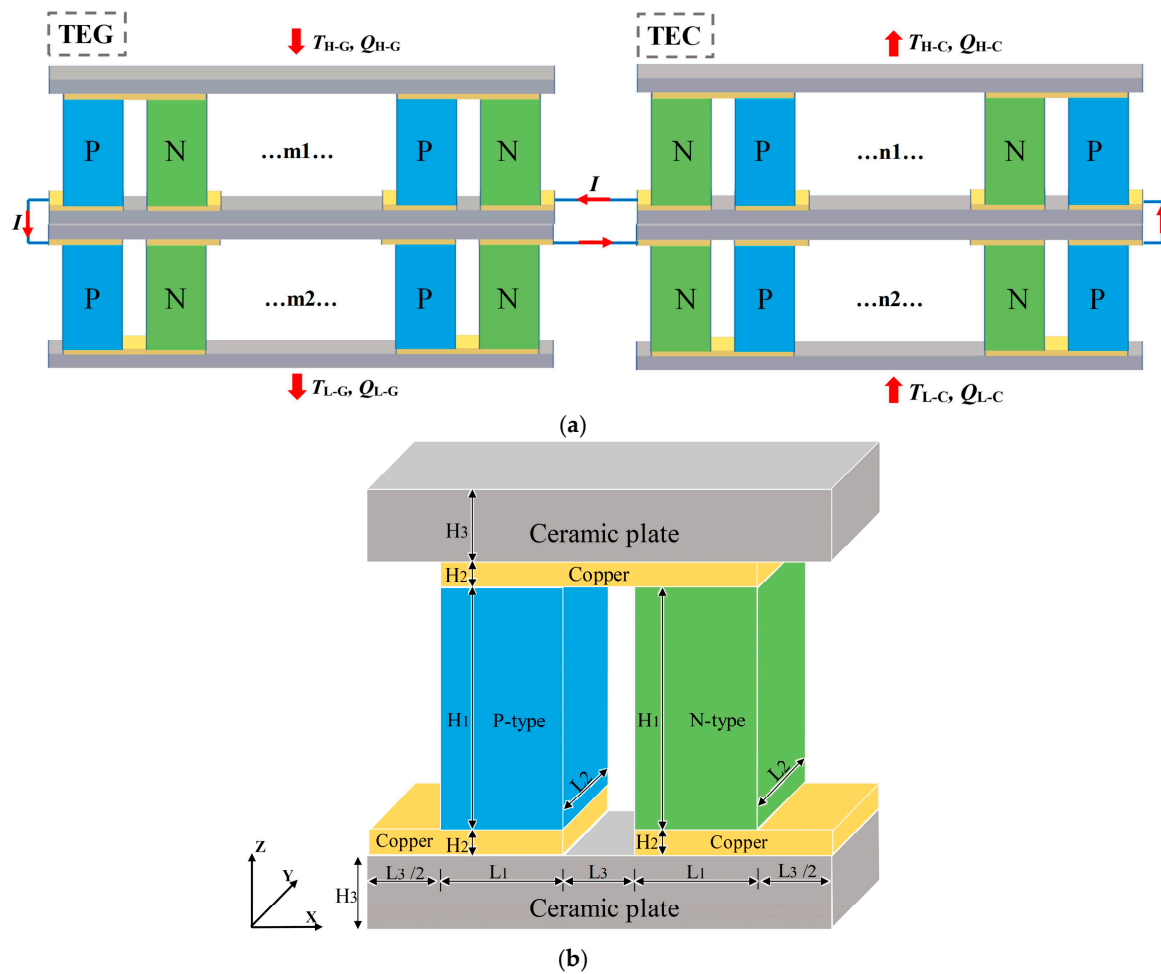
Figure 1. (**a**) Schematic diagram of the two-stage CTE; (**b**) Schematic diagram thermoelectric element of the CTE.

Table 2. Geometry structure of thermoelectric elements.

Geometry of Thermoelectric Elements [9]		
L_1 = 1.0 mm	L_2 = 1.0 mm	L_3 = 0.2 mm
H_1 = 1.0 mm	H_2 = 0.1 mm	H_3 = 0.3 mm

2.2. Material Properties

The properties of thermoelectric materials are specified as temperature-dependent and formulated as follows, where α denotes the Seebeck coefficient (V K^{-1}), k denotes the thermal conductivity (W m^{-1} K^{-1}), and ρ denotes electric resistivity (Ω m). For the p-type leg [11]:

$$\alpha_p = \left(22,224 + 930.6T - 0.9905T^2\right) \times 10^{-9} \text{ V K}^{-1} \tag{1}$$

$$k_p = \left(62,605 - 277.7T + 0.4131T^2\right) \times 10^{-4} \text{ W m}^{-1} \text{ K}^{-1} \tag{2}$$

$$\rho_p = \left(5112 + 163.4T + 0.6279T^2\right) \times 10^{-10} \ \Omega \text{ m} \tag{3}$$

For the n-type leg [11]:

$$\alpha_n = -\left(22,224 + 930.6T - 0.9905T^2\right) \times 10^{-9} \text{ V K}^{-1} \tag{4}$$

$$k_{\mathrm{n}} \;=\; \left(62,605 - 277.7T + 0.4131T^2\right) \times 10^{-4} \ \mathrm{W\ m^{-1}\ K^{-1}} \tag{5}$$

$$\rho_{\mathrm{n}} \;=\; \left(5112 + 163.4T + 0.6279T^2\right) \times 10^{-10} \ \Omega\ \mathrm{m} \tag{6}$$

Besides, the Seebeck coefficient α_{Cu}, thermal conductivity k_{Cu}, and electric resistivity ρ_{Cu} for the copper connectors are specified as constants of 6.5×10^{-6} V K^{-1}, 400 W m^{-1} K^{-1}, and 1.7×10^{-9} Ω m, respectively. The thermal conductivity of the ceramic plate k_{Ce} is specified as 175 W m^{-1} K^{-1}. It should be indicated here that, a new thermal conductivity value of Al$_2$O$_3$ ceramics was reported recently by Yoo et al. [43]. The thermal conductivity decreases with temperature and is formulated as follows:

$$k_{\mathrm{Ce}} \;=\; \left(573,275 - 2037.1T + 3T^2 - 0.00156T^3\right) \times 10^{-4} \ \mathrm{W\ m^{-1}\ K^{-1}} \tag{7}$$

It is believed that the device performance is sensitive to the thermal conductivity of the ceramic plate because it is a key component in the device. Adoption of Equation (7) is more practical because it is temperature-dependent. To justify this, simulations with the updated thermal conductivity are also performed. The comparison of the results calculated by using the values of 175 W m^{-1} K^{-1} and Equation (7) are shown in Figure A1 from Appendix A. We can conclude that the previous studies using the constant thermal conductivity of 175 W m^{-1} K^{-1} overestimate the device performance. However, for convenience to compare our optimization results with those reported in previous publications, the following results are calculated by using a constant thermal conductivity value of 175 W m^{-1} K^{-1}.

2.3. Governing Equations

When an external heat source is loaded on the TEG, the heat-driven carriers of holes and electrons migrate from the hot end to the cold end across the device. A current is generated as a result. When an electric current is injected into the TEC, carrier-driven heat is pumped from the cold end to the hot end. It has been demonstrated that while the TEG or TEC operates, the Seebeck effect, Peltier effect, and Thomson effect co-exist and are accompanied by a Joule heating effect, heat conduction effect, and electric conduction effect. Under this circumstance, the electric current, electric potential, temperature, electric field are all multi-physically coupled with each other. Hence, a 3D multi-physics complex coupling thermoelectric model developed by our previous work [9,12,44,45] is adopted as the direct problem solver in the present study. To facilitate solving the model, the following assumptions are adopted: (1) the electric and thermal contact resistances between thermoelectric couple/metallic connector and metallic connector/ceramic plate are neglected; (2) the radiative heat loss and convective heat transfer loss to the environment are not of concern.

The governing equations determining the physics of CTE are expressed as follows. For brevity, a general form of energy equation for the p-type leg, n-type leg, metallic connector, and ceramic plate reads:

$$\nabla \cdot (k_i \nabla T) \;+\; \frac{J^2}{\sigma_i} - \beta_i \vec{J} \cdot \nabla T \;=\; 0 \tag{8}$$

where T denotes absolute temperature, $\vec{J}$ represents current density vector, k is thermal conductivity, σ denotes electric conductivity, and β means the Thomson coefficient which is expressed as:

$$\beta \;=\; T \frac{d\alpha}{dT} \tag{9}$$

where α is the Seebeck coefficient. The first term on the left side of Equation (8) represents Fourier's heat conduction effect, the second term describes the Joule heating as internal heat sources, and the third term is the Thomson effect. It is noted that the second and third terms in Equation (8) both diminish for the ceramic plates because of their electrical insulation. The electric potential profile is solved by the following formula:

$$\nabla \cdot (\sigma(\nabla \psi - \alpha \nabla T)) \;=\; 0 \tag{10}$$

where ψ denotes the electric potential, $\alpha\nabla T$ denotes the thermoelectric electromotive force driven by the Seebeck effect. After the profile of ψ is obtained the electric field can be solved by the following equation:

$$\vec{E} \;=\; -\nabla\psi + \alpha\nabla T \tag{11}$$

Finally, the current density can be obtained through Ohm's law:

$$\vec{J} \;=\; \sigma\vec{E} \tag{12}$$

More details of the modeling can be found in [9,12,44,45]

2.4. Boundary Conditions

Four temperatures employed in the present CTE device are defined as follows: $T_{\text{H-G}}$ is the temperature at the hot end of the top stage in TEG; $T_{\text{L-G}}$ is the temperature at the cold end of the lower stage in TEG. $T_{\text{H-C}}$ is the temperature at the hot end of the top stage in TEC; $T_{\text{L-C}}$ is the temperature at the cold end of the lower stage in TEC. In the simulation, $T_{\text{H-G}} = 450$ K, $T_{\text{L-G}} = 300$ K, $T_{\text{H-C}} = T_{\text{L-C}} = 300$ K.

Note that $T_{\text{H-C}} = T_{\text{L-C}} = 300$ K is a particular case in TEC model. In common practical applications, however, TECs usually operate with $T_{\text{H-C}} - T_{\text{L-C}} > 0$. Wang et al. [9,12] have proved that $Q_{\text{L-C}}$ increases with decreasing temperature difference of $T_{\text{H-C}} - T_{\text{L-C}}$ under the same injection current (see Figure 5 in [9] and Figure 9 in [12]). Consequently, $Q_{\text{L-C}}$ will reach its maximum value when $T_{\text{H-C}} - T_{\text{L-C}} = 0$ K. To obtain a maximum of $Q_{\text{L-C}}$, $T_{\text{H-C}} = T_{\text{L-C}} = 300$ K is adopted in the present work. However, to examine the effect of different $T_{\text{H-C}} - T_{\text{L-C}}$ temperature differences on the device performance, simulations with $T_{\text{H-C}} - T_{\text{L-C}} = 20$ K are also performed and the results are shown in Table A1 and Figure A2 from Appendix B. The data will be discussed and compared with the literature later.

On the side surfaces of the TEG and TEC element, the adiabatic boundary conditions are specified as follows:

$$\frac{\partial T}{\partial z} \;=\; 0 \tag{13}$$

where, z denotes the component with direction normal to the side surface of the device. On the internal interfaces between adjacent materials, the temperature and heat flux are assumed continuous.

For the electric modeling module, the TEC module is specified as the load of the TEG module. The outlet of current for the TEC is directly connected with the inlet of current of the TEG. On the other surfaces of the CTE element, the current cannot flow out:

$$\vec{J} \cdot \vec{z} \;=\; 0 \tag{14}$$

where $\vec{z}$ denotes the element vector normal to the side surface of the device.

2.5. The CTE Performance Metrics

In the present study, the performance of the TEG-TEC combined system is evaluated by the following two objective functions defined as:

$$f_1(n_1, n_2, m_1, m_2) \;=\; Q_{\text{L-C}} \tag{15}$$

$$f_2(n_1, n_2, m_1, m_2) \;=\; \text{COP} \;=\; \frac{Q_{\text{L-C}}}{Q_{\text{H-G}}} \tag{16}$$

where $Q_{\text{L-C}}$ is the absorbed heat pumped from the cold end of the lower stage in TEC, and $Q_{\text{H-G}}$ is the total heat supplied from the hot end of the top stage in TEG.

The governing Equations (8)–(12) are iteratively solved to determine the temperature distributions and electric potential profile in the CTE. When the temperature difference across the TEG is established,

the heat flux will be driven from the hot end on the top stage to the cold end on the lower stage of the TEG. Then, the value of $Q_{\text{H-G}}$ can be determined. Meanwhile, the current generated in the TEG is injected into the TEC to pump heat by the Peltier effect. When the current flowing through the TEC is known, $Q_{\text{L-C}}$ can be determined at the interface between copper connectors and semiconductors by using the formula αTJA (Peltier effect), where A is the cross-sectional area at the interface. Finally, the COP can be calculated.

3. Optimization Procedure

3.1. Multi-Objective Functions and Optimization Algorithm

The performance metrics to evaluate a CTE module contains cooling capacity and COP, which are calculated by Equation (15) and Equation (16), respectively. In general, these two indicators cannot reach their maximum values simultaneously, which means a higher cooling capacity always is at the cost of a deteriorated COP. This general conclusion will be demonstrated by the present calculated data later. Thus, it is difficult to obtain an ideal solution to a particular practical application.

To resolve this contradiction, multi-objective optimization is necessary. The classical solution to this problem is converting multiple objectives into a single composite function expressed as:

$$\text{Max } f(n_1, n_2, m_1, m_2) = \omega_1 \cdot \{\frac{f_1(n_1, n_2, m_1, m_2)}{f_1{}^{\max}}\} + \omega_2 \cdot \{\frac{f_2(n_1, n_2, m_1, m_2)}{f_2{}^{\max}}\} \tag{17}$$

where ω_1 and ω_2 are artificially specified weight factors. In this way, the optimization results are sensitive to the weight factors ω_1 and ω_2. Thus, the results are not always the ideal solutions, because they are always accompanied by subjective empirical errors.

To avoid this problem, a Non-dominated Sorting Genetic Algorithm II (NSGA-II) [46] is adopted in the present work. It should be indicated that the encoding method in this algorithm is changed to binary because of the integer optimization variables requirement. NSGA-II is a popular fast elitist multi-objective and non-domination-based genetic algorithm. The principle of NSGA-II can be described as follows: first, a population with size N is initialized. After non-dominated sorting, a new hierarchy of sub-populations was generated through genetic selection, intercross, and variation. From the second generation, the algorithm preserves and use the best solutions found previously in subsequent generations. Then, a non-dominated sorting and crowded tournament selection are performed to preserve the diversity among non-dominated solutions in the later stage of the run, in which way it can obtain a good spread of solutions. Finally, a new hierarchy of sub-populations was generated, loop, and until the well-spread solutions over the Pareto-optimal front are found.

The entire optimization procedure is shown in Figure 2, where in this work the population size N is 40 and the evolutionary generation is 80. The detailed numerical and structural parameters of the optimization algorithm are given in Tables A2 and A3 from Appendix C.

In the optimization procedure, the design parameters contain four variables m_1, m_2, n_1, and n_2. The design variables are subjected to the following constraint:

$$\begin{cases} m_1 + m_2 + n_1 + n_2 = 40 \\ 1 \leq m_1, m_2, n_1, n_2 \leq 37 \\ m_1, m_2, n_1, n_2 \subseteq \text{N}^* \end{cases} \tag{18}$$

where N* means positive integers. In this optimization method, the Pareto front indicates any arbitrary compromise between the maximum cooling capacity and COP. The concept of Pareto frontier is shown in Figure 3. In the optimization procedure, the individuals (the definition can be found in [13–15]; it means any point to which a user can apply the objective function) are sorted according to the objective function values. In the following evolution steps, non-dominated solutions with higher fitness score

are more likely to be adopted and preserved. Therefore, as the iterative process continues, the Pareto optimal solutions will be evolved gradually until the Pareto front is obtained.
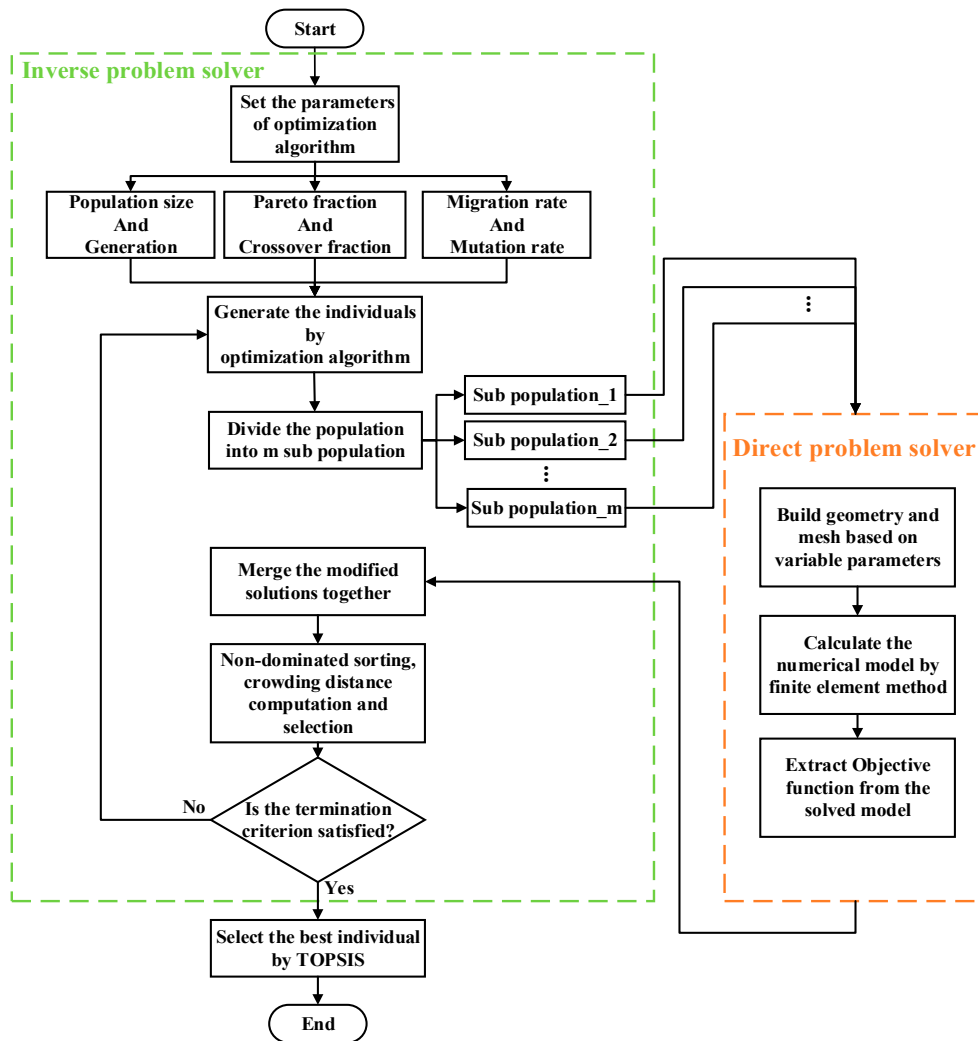

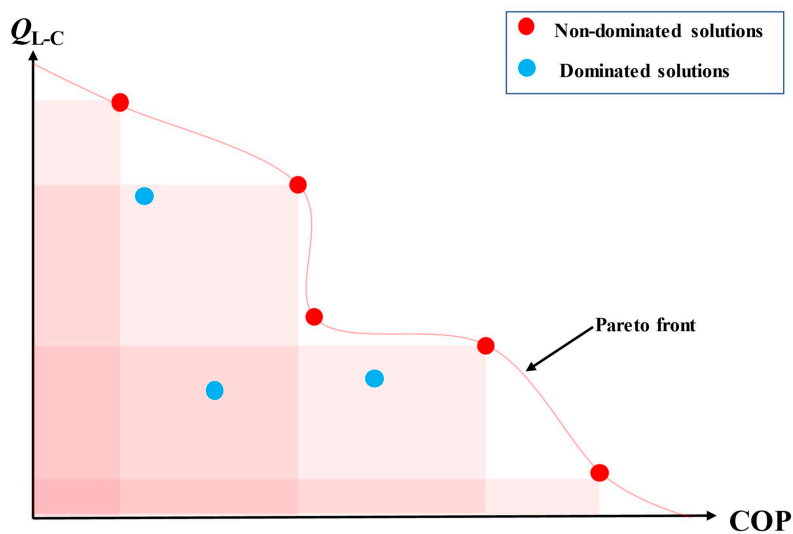**Figure 2.** Flowchart of the optimization procedure.

Figure 3. Schematic of the Pareto concept.

3.2. TOPSIS Selection

For practical applications, it is important to choose the best alternatives among several solutions. However, the best alternatives cannot be obtained by sorting the fitness function values in the Pareto solution set, because solutions from the Pareto frontier have the same level of optimization. Therefore, a decision-making approach is necessary to select the best solution from the alternatives. In the present multi-objective optimization, a classic and practical decision-making method, TOPSIS, is used and is expected to provide a reasonable compromise solution [47]. It selects alternatives closest to the ideal solution and farthest from the negative-ideal solution. The procedure of the TOPSIS method can be divided into following six steps:

Step 1: Measure the normalized decision matrix. The normalized value r_{ij} is:

$$r_{ij} = \frac{x_{ij}}{\sqrt{\sum\limits_{i=1}^{m} x_{ij}^2}}$$

$$i = 1, 2, \ldots, m \text{ and } j = 1, 2, \ldots, n \tag{19}$$

where x_{ij} denotes the performance measure of the *i*-th alternative solution in terms of the *j*-th objective.

Step 2: Specify the weight coefficient w_j and measure the weighted normalized decision matrix. The weighted normalized value v_{ij} is:

$$v_{ij} = r_{ij} \times w_j$$

$$i = 1, 2, \ldots, m \text{ and } j = 1, 2, \ldots, n \tag{20}$$

where w_j is the weight of the Jth criterion or attribute and $\sum_{j=1}^{n} w_j = 1$. Here, the weight factors assigned to Q_{L-C} and COP are 0.65 and 0.35 respectively, which means the interested application requires a relative high Q_{L-C} and a not too much low COP.

Step 3: Determine the positive ideal solution A^+ and negative ideal solution A^-:

$$A^+ = \{(\max_i v_{ij} | j \in C_b), (\min_i v_{ij} | j \in C_c)\} = \{v_j^+ | j = 1, 2, \ldots, n\} \tag{21}$$

$$A^- = \{(\min_i v_{ij} | j \in C_b), (\max_i v_{ij} | j \in C_c)\} = \{v_j^- | j = 1, 2, \ldots, n\} \tag{22}$$

Step 4: Measure the separation metrics with the *n*-dimensional Euclidean distance. The separation metrics for each alternative solution from the positive ideal solution and the negative ideal solution are as follows:

$$S_i^+ = \sqrt{\sum\limits_{j=1}^{n} (v_{ij} - v_j^+)^2} \tag{23}$$

$$S_i^- = \sqrt{\sum\limits_{j=1}^{n} (v_{ij} - v_j^-)^2} \tag{24}$$

Step 5: Measure the relative closeness to the ideal solution. The relative closeness of the alternative A_i to ideal solution A^+ is defined as:

$$RC_i^+ = \frac{S_i^-}{S_i^+ + S_i^-} | i = 1, 2, \ldots, m \tag{25}$$

Step 6: Rank the preference order of each solution by relative closeness, and select the one which is the shortest to the ideal solution.

Note that, the TOPSIS method also applies a weight factor according to Equation (20), which is similar to the classical solution expressed in Equation (17). Thus, to definite the advantages of the present method, further discussion about the above two methods is necessary.

3.3. Comparison between Preference-based Method and Ideal Method

There are two methods to perform multi-objective optimization [48], the procedures of which are illustrated in Figure 4. One is the preference-based strategy according to Equation (17). It converts multiple objectives into a single composite one by specifying relevant preference weight factors. This method obtains a single trade-off solution by a single-objective optimization algorithm. Because preference weight factors are first determined based on high-level information before optimization, we call this method the preference-based multi-objective optimization. For the TOPSIS method used in the present study, a user can use multi-criteria decision-making methods to choose an ideal alternative after a set of trade-off optimal solutions are found. We call this method the ideal multi-objective optimization. Although the classical method and the TOPSIS method both need to specify weight factors, there are still some fundamental differences between both approaches:

(1) For the preference-based method, a relevant preference weight factor is required to be specified before the optimal solution is obtained. This requires analysis of experience-driven information to determine a proper preference vector. However, this is a difficult task without any knowledge of the possible trade-off solutions, unless an accurate and reliable preference weigh factor is available. Consequently, the optimal solution obtained by such method is highly subjective to the particular user. On the contrary, for the ideal approach, a user does not need any relevant preference weigh factor information before optimization. Once a well-distributed set of trade-off solutions is found, the problem information is easy to be used to choose an alternative with the knowledge of already obtained trade-off solutions. Thus, the ideal approach is less subjective as well as more methodical and more practical.

(2) For the preference-based method, the optimized solution obtained by the preference-based strategy is sensitive to the weight factors forming the composite objective. A change in this preference vector inevitably results in a different trade-off solution. If the preference driven by practical applications is changed, a new search for a new solution is required. Consequently, to find multiple trade-off solutions, procedure-repeating with different weight factors is required, which is time-consuming and impractical. On the contrary, for the ideal approach, when objective preference is changed, it is not needed to search for a new solution; instead, it only need to choose another alternative from a set of already obtained trade-off solutions by considering high-level information. It is not needed to be performed many times to find multiple ideal solutions, which greatly increases the flexibility of the optimization procedure and saving time.
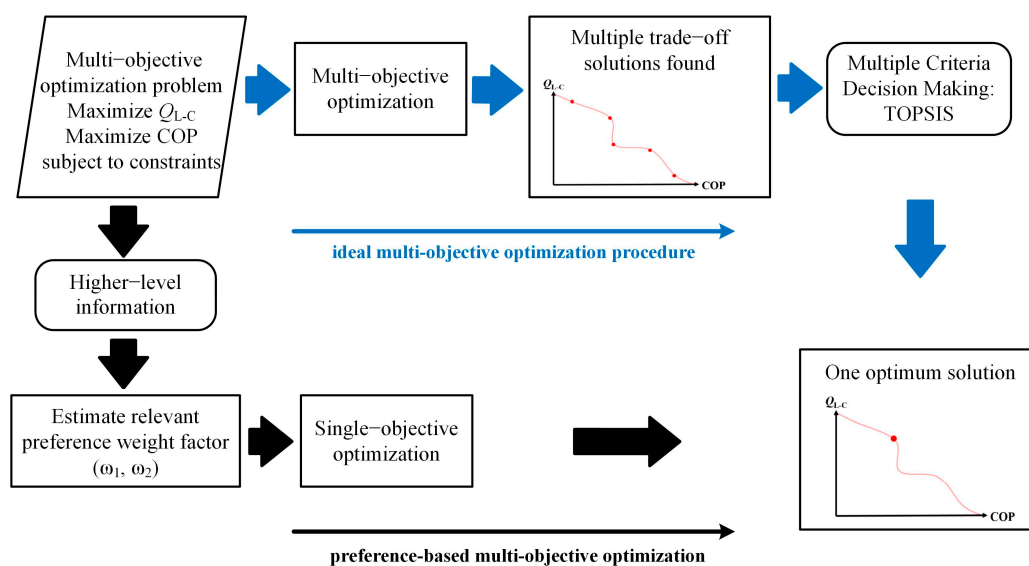

Figure 4. Schematic of the preference-based and ideal multi-objective optimization approaches.

Looking back to the two objective functions used in Equations (15) and (16), generally, for CTE, the decision-making is driven by the practical application requirements. For example, when the CTE is used to generate power by waste heat, a very high Q_{L-C} and a not too low COP would be of interest, because the Q_{H-G} flux would be wasted anyway. On the contrary, when the CTE is applied in a severe environment where power is lacking (such as aerospace applications), a very high COP is necessary, and Q_{L-C} becomes a less important factor of concern.

4. Results and Discussion

4.1. Model Validation

Before model validation, a grid sensitivity examination is performed to ensure the calculated results are independent of the grid. Three sets of grids are examined, as shown in Table 3. In the test, $T_{H-G} = 450$ K, $T_{L-G} = T_{H-C} = T_{L-C} = 300$ K, $m_1 = m_2 = n_1 = n_2 = 10$. The cooling capacity and COP calculated by different grids are shown in Table 3. It is evident that the relative errors for Q_{L-C} and COP are 5.59×10^{-5} and 2.39×10^{-5} respectively when compared between Grid 2 and Grid 3, which means that these two sets grids are valid. To simultaneously ensure the accuracy and save computational time, Gird 2 is selected in the present work. The characteristics of the grid used are shown in Figure 5.

Table 3. Grid independence test with element allocation ($m_1 = m_2 = n_1 = n_2 = 10$).

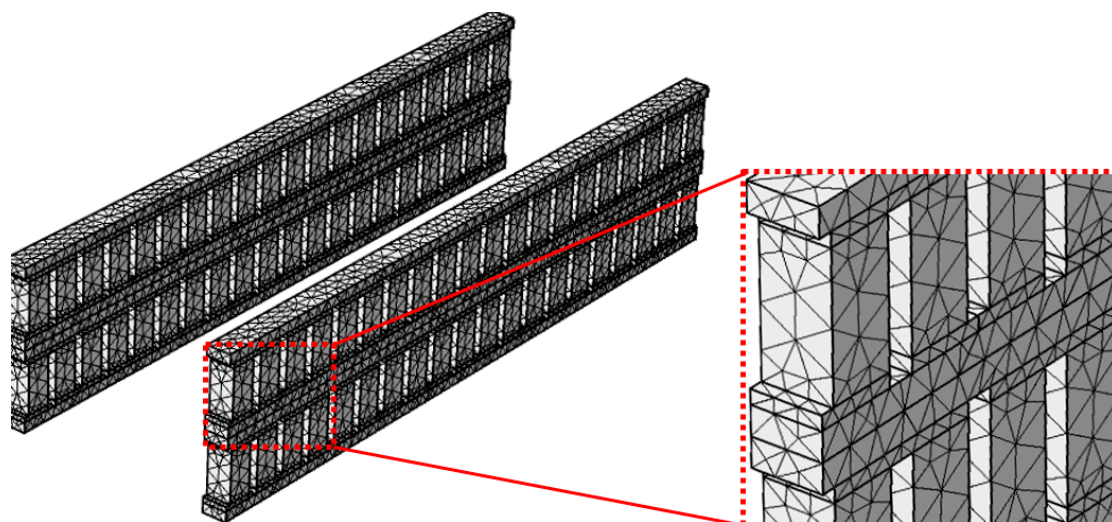| Grid Sets	Degrees-of-Freedom	Q_{L-C} (W)	Error	COP	Error
Grid 1	21,942	0.17897	1.68×10^{-4}	0.190692	5.04×10^{-5}
Grid 2	159,259	0.17895	5.59×10^{-5}	0.190684	2.39×10^{-5}
Grid 3	638,759	0.17894		0.190682	

Figure 5. The characteristics of the grid used is the simulation.

To validate the present model, a results comparison according to *I-U* curves between Hu et al.'s report [49] and the present simulations is carried out. In [49], the TEG comprises an N-type semiconductor leg of Bi_2Te_3 with dimensions of $2.98 \times 2.215 \times 6.22$ mm^3 and copper connectors. The performance of the TEG was numerically and experimentally examined. Temperature conditions for the hot end were set as 423 K, while the cold end was maintained at room temperature. For fair comparison, the operation condition and geometry simulated by the present model keep identical to those used in [49]. Figure 6 shows the variation of *I-U* curves between the present model and Hu et al.'s report. It is evident that the simulation results agree well with Hu et al.'s work, except for a slightly overestimation of the output voltage at large output currents. The maximum deviation is less than 3%.

The ignored contact electrical resistance and thermal resistance are responsible for the discrepancy between the simulations and experiments.
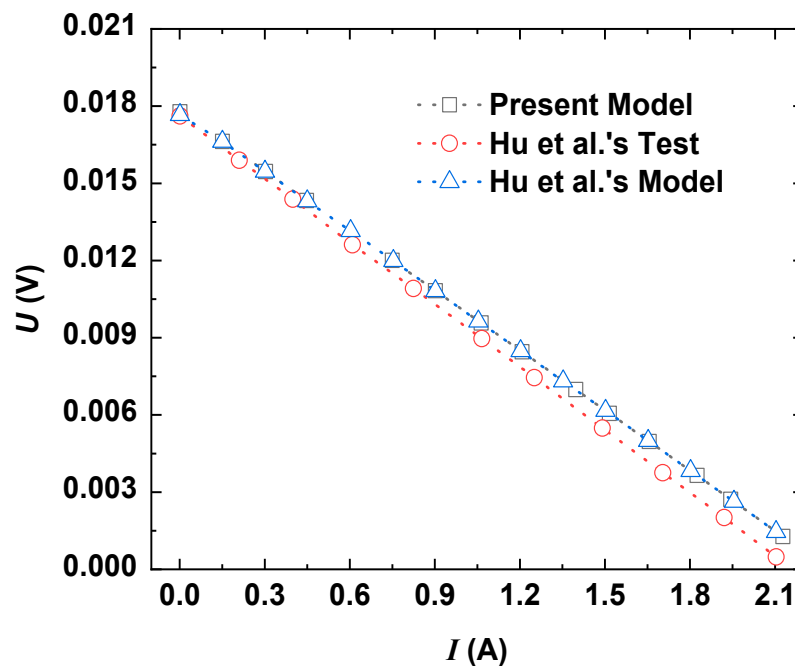

Figure 6. Results comparison according to *I-U* curves between Hu et al.'s report [49] and the present simulations.

4.2. Optimization Results

Figure 7 shows the optimization evolution progress. The first, fourth, tenth and eightieth generations are present in Figure 6a–d, respectively. It proves that the solution converges at the tenth generation. To get a more accurate solution set, the solutions of the eightieth generation was selected in the present study. It should be indicated that, to ensure the trade-off solutions over the Pareto front are independent of the initial variable values randomly generated at the begin of the running, three sets of populations were determined. The results show that they are converted into a single Pareto front (see in Figure 7d). This strongly justifies the effectiveness of the simulated results. Figure 8 shows the Pareto front after multi-objective optimization, where the solutions are shown non-dominated. In the optimization process, Q_{L-C} ranges from 0.06 to 0.18 and COP increases from 0.24 to 0.63. After determining the positive ideal solution ($Q_{L-C} = 0.18$ and COP = 0.63) and negative ideal solution ($Q_{L-C} = 0.06$ and COP = 0.24), the TOPSIS optimal results can be obtained at $Q_{L-C} = 0.16$ and COP = 0.36, respectively. The value of the corresponding variables of m_1, m_2, n_1, and n_2 are 5, 6, 15, and 14 respectively. The value of search variables and performance metrics corresponding to each individual over the Pareto front for the improved CTE system is listed in Table A4 from Appendix C.

As indicated in the temperature boundary condition section, the simulations with $T_{H-C} - T_{L-C} = 20$ K is more practical with a view to commercial application. The results of this case are shown in Appendix B. It should be noted here that the thermal conductivity of the ceramic plate is set as Equation (7) because temperature-dependent property is more practical. Table A1 lists the value of search variables of n_1, n_2, m_1, and m_2 and performance metrics for the improved CTE system. The temperature profiles of five different allocation design with different sets of n_1, n_2, m_1, and m_2 are shown in Figure A2. It is found that the optimal design is reached with a ratio of elements number between stages greater than 1, which is consistent with the results reported by Xuan et al. [50].
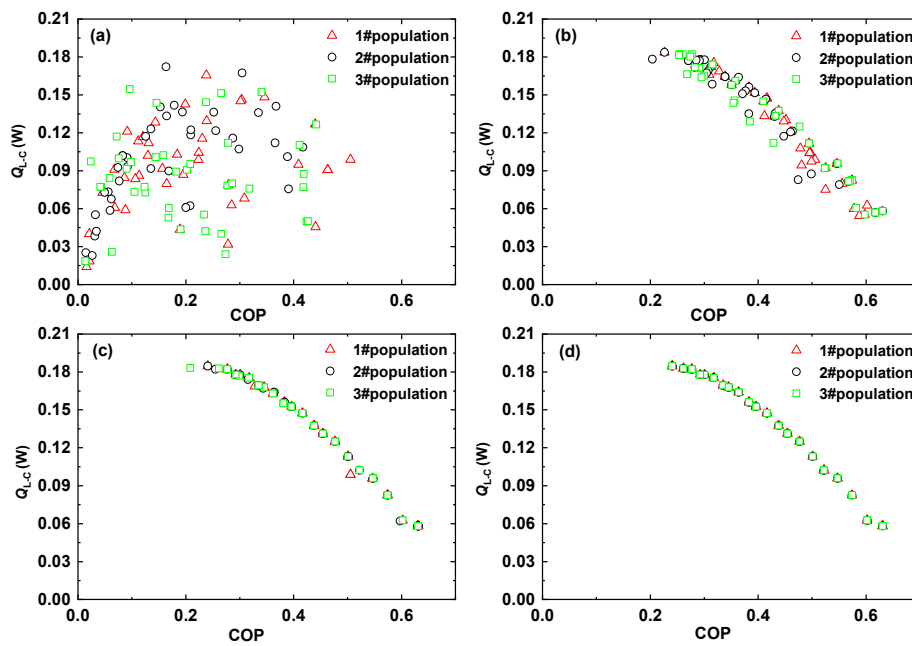
Figure 7. Distribution of Pareto fronts with three different populations: (**a**) the first generation; (**b**) the fourth generation; (**c**) the tenth generation; and (**d**) the eightieth generation.
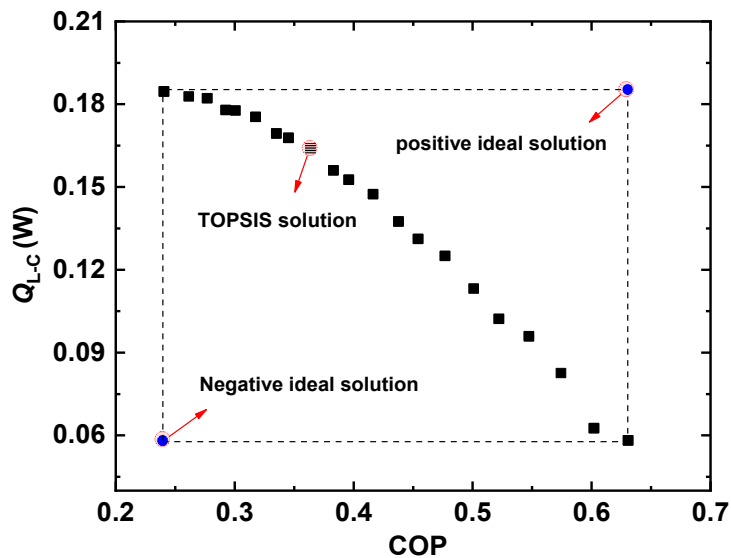

Figure 8. The set of trade-off solutions over Pareto front with ideal solution selected by TOPSIS.

Figure 9 illustrates the optimized element number assigned to each stage for each alternative solution along the Pareto front. It can be found that for each Pareto solution, number of elements of the TEC is always more than that of the TEG. The reason is that the TEC module must reject the extra Joule heat generated during TEC operation, which is not required in the TEG module. For TECs or TEGs considered individually, the element number for each stage shows less difference. Some solutions even show that each stage has the same element number either for the TEG or the TEC. When each stage shares a different element number, the number of elements in the top stage is larger than that of the lower stage for the TEC. On the contrary, the number of elements in the top stage is smaller than that in the lower stage for the TEG. These results are attributed to the fact that either for the TEC or the TEG, the heat rejection stage needs more elements to pump the extra Joule heat. The results reported by Xuan et al. [50] are qualitatively consistent with above results, where it demonstrated that

the maximum $Q_{L\text{-}C}$ (as well as the optimum COP) is reached with a number ratio of elements between stages greater than 1.
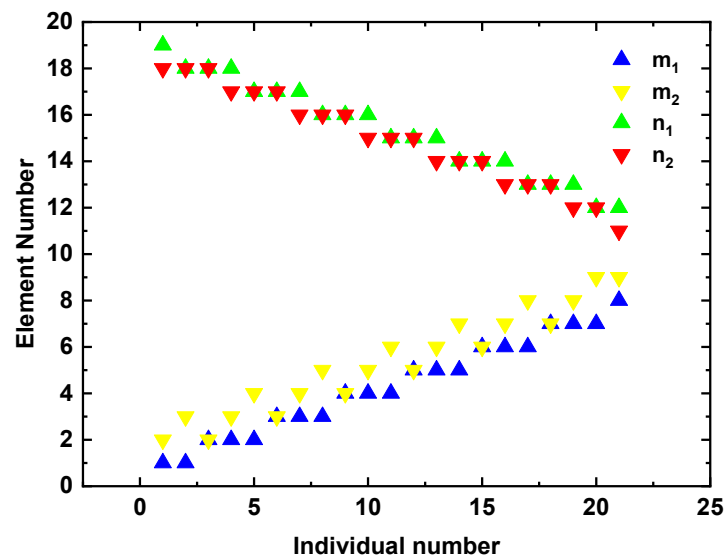

Figure 9. Allocation of element number to each stage in different individual number.

Figure 10a–b show the optimized objective functions of $Q_{L\text{-}C}$ and COP in the Pareto-optimal solution set. As the alternative solution varies, $Q_{L\text{-}C}$ increases from 0.06 to 0.18 and the corresponding COP decreases from 0.63 to 0.24, respectively. In addition, the variation of current is another indicator to evaluate the performance of the device. From Figure 10c, it can be concluded that the current increases from 0.03 A to 0.14 A over the Pareto front. This means more Joule heat will be generated, which enhances the load for pumping heat from the cold end. The element number allocation shown in Figure 9 can verify these results. The increased current accompanies more thermoelectric elements assigned to the TEG. The increased current can enhance $Q_{L\text{-}C}$; however, the number allocated to the TEC module are also decreased which deteriorates $Q_{L\text{-}C}$. There exists a trade-off between the above two factors to determine the final $Q_{L\text{-}C}$. The enhanced $Q_{L\text{-}C}$ with increasing current demonstrates that the effect of electric current to increase $Q_{L\text{-}C}$ is stronger.

To verify the advantage of the optimized design, reference structure should be defined for performance comparison. NSGA-II algorithm begins with an initialized generation comprised of a collection of individuals generated randomly, any one of these individuals can be marked as an initial structure. As the optimization procedure evolves, the population searches fitter and fitter solutions by new generations and eventually converges to a set of Pareto-optimal solutions. Based on this principle, without the knowledge of how to determine the relevant values of m_1, m_2, n_1, and n_2 to design a CTE with optimal performance, values randomly specified as m_1, m_2, n_1, and n_2 seem to be an intuitive method. Hence, the initial structure randomly generated in the first generation can be marked as a benchmark to compare. To ensure the reliability of the reference structure, the three randomly generated initial structures corresponding to populations 1#, 2#, and 3# shown in Figure 7 are all selected, which are marked as 1# initial solution, 2# initial solution, and 3# initial solution, respectively. It should be noted that, another case that can also be intuitively selected as reference is the equal allocation to m_1, m_2, n_1, and n_2. Thus, this case is also selected as the benchmark to compare.
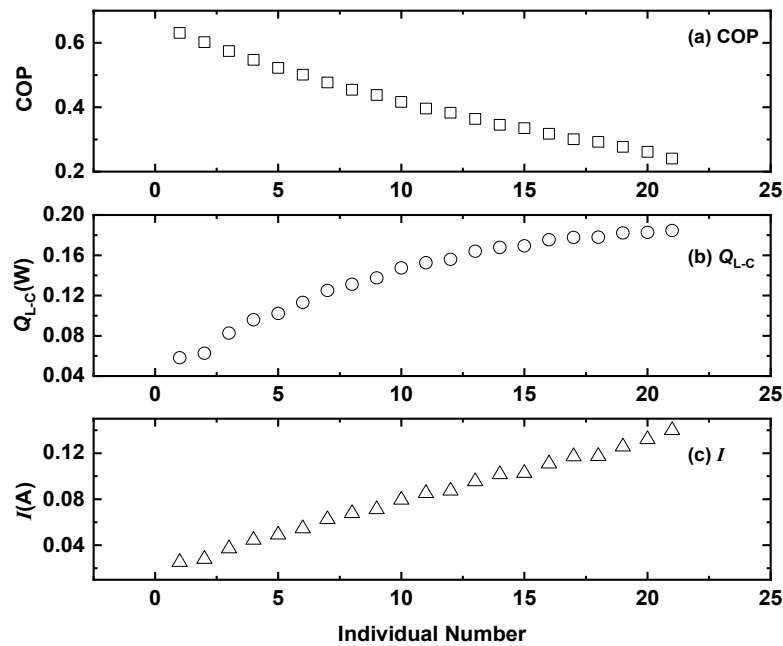
Figure 10. Performance variation with different individual solution: (**a**) cooling capacity; (**b**) COP; and (**c**) electrical current.

The values of the objective functions compared between the three initial solutions and the optimized design selected by TOPSIS are shown in Figure 11. The equal allocation design is also compared in the figure. From Table 4, it is worth mentioning that, after optimization, the cooling capacity is improved by 23.3%, 90.2%, and 551.7%, respectively, compared with 1# initial solution, 2# initial solution, and 3# initial solution. COP is increased by 122.0%, 221.1%, and 2377.4%, respectively, compared with 1# initial solution, 2# initial solution, and 3# initial solution. Also, it can be found that the optimized design has increased COP by 90.6% at the expense of 8.1% cooling capacity compared to equal allocation design. In terms of comprehensive trade-offs between cooling capacity and COP, the optimized design selected by TOPSIS is superior to both initial design and equal allocation design structure.
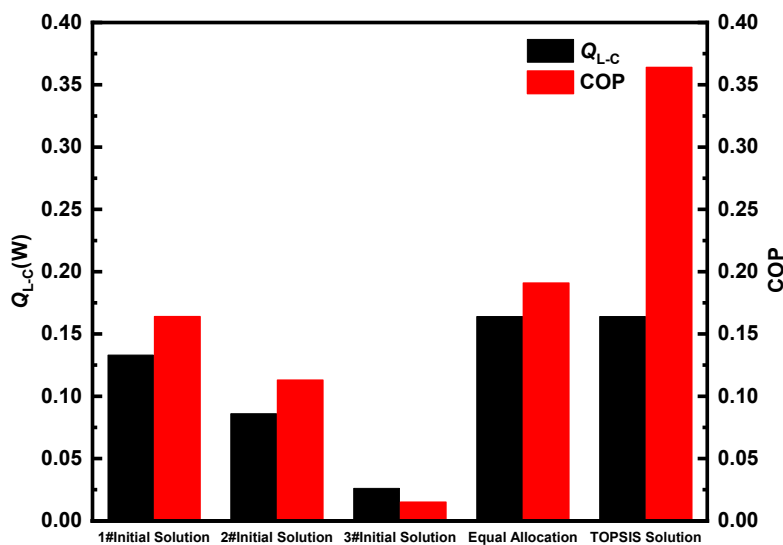

Figure 11. Performance metrics comparison between the three initial solutions, the equal allocation design, and the optimized design.

Table 4. Parameters and performances comparison between the Initial Solutions, Equal Allocation, and TOPSIS Solution.

Reference Structures	Allocation				Q_{L-C}(W)	Variation	COP	Variation
	m_1	m_2	n_1	n_2				
1#Initial Solution	7	14	7	12	0.133	23.3%	0.164	122.0%
2#Initial Solution	5	16	7	12	0.086	90.2%	0.113	221.1%
3#Initial Solution	1	3	21	15	0.025	551.7%	0.015	2377.4%
Equal Allocation	10	10	10	10	0.179	−8.4%	0.191	90.6%
TOPSIS Solution	5	6	15	14	0.164	-	0.364	-

To explain the underline physics of the improved performance for the optimized structure, the temperature profiles of the improved design is compared with the three initial solutions and the equal allocation design as shown in Figure 12. It is found that the temperature difference is very large between the top and lower stages for both the TEG and the TEC module in the three initial solutions, which means the heat cannot transfer easily through the device due to the improper element number allocation. The heat is accumulated at the interface between the top and the lower stage in the TEC module. For the equal allocation design, although the heat transport is more uniform, there still exist heat accumulation. However, after optimization, appropriate element number ratio between the TEG and TEC as well as between the two stages for TEG and TEC eliminate the heat accumulated at the stage interfaces, which enhance the entire performance of the CTE. This mechanism is consistent with the previous results reported in [51].

To further elucidate the effect of variation of m_1, m_2, n_1, and n_2 on the performance of the CTE device, analysis from the point of view of temperature distribution and heat flux is present in this section. the results are beneficial to optimize the geometry of the device. It is believed that when the element number allocated to TEG is fixed, different number ratio between the top and the lower stage of TEC will influence the CTE performance, and vice versa when the element number allocated to TEC is fixed. Also, when the element number allocated to the two lower stages of CTE is fixed, different number ratio between the TEG module and the TEC module for the two top stages of CTE will influence the CTE performance, and vice versa when the element number allocated to the two top stages of CTE is fixed. Accordingly, four sets of cases corresponding to above conditions are shown in Figure 13a–d, respectively, in which the variables of n_1, n_2, m_1, and m_2 are changed, respectively. It is interestingly found that, for each variable, there exists an optimal value, which corresponding to the optimal solution selected by TOPSIS in the optimization procedure.

The heat transport equilibrium between the TEG module and the TEC module or between the top stage and the lower stage of the CTE is the key point to determine the device performance. To justify this hypothesis, we select the cases shown in Figure 13a as representatives to analyze, where the structures with n_1 = 5, 11, 15, 19, and 25 are chosen. When the elements to the top and the lower stage of TEC are re-allocated, the circuit load connected to the TEG is changed, which may cause the generated current decrease or increase. Then the Joule heat and Q_{L-C} curve vary with current. Besides, the re-allocated elements also leads to the heat load to the top and the lower stage changed, breaking the heat transport equilibrium in the device. The updated cooling capacity of the top and the lower stage influence Q_{L-C}. Above factors together determine the final Q_{L-C}. The temperature profiles and heat flux distributions are illustrated in Figures 14 and 15, respectively. It is found that, as n_1, increases from 3 to 15, the heat accumulated at the interface is alleviated, and the heat flux is also distributed more uniformly. As n_1 further increases from 15 to 25, the heat flux distribution and the resultant temperature profile is again deteriorated. The change of heat transport equilibrium influences the Q_{L-C} of the TEC and the Q_{H-G} of the TEG, which resultantly causes the COP variation.
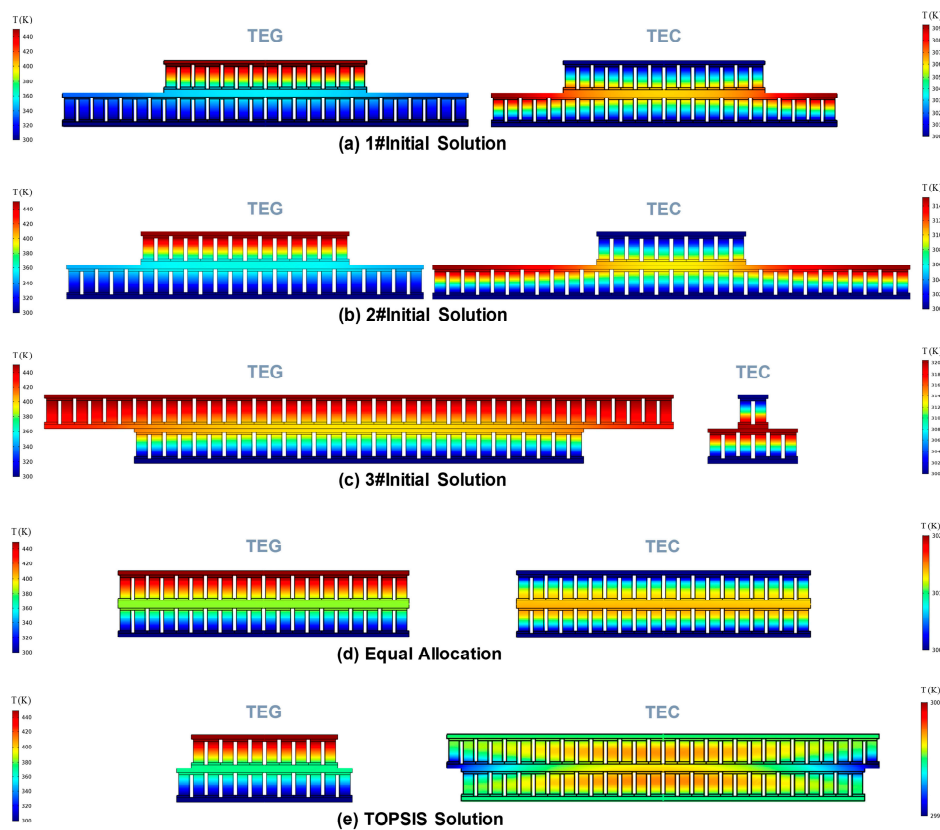
Figure 12. Temperature profiles of different allocation design: (**a**) 1# Initial Solution; (**b**) 2# Initial Solution; (**c**) 3# Initial Solution; (**d**) Equal Allocation; and (**e**) TOPSIS Solution.
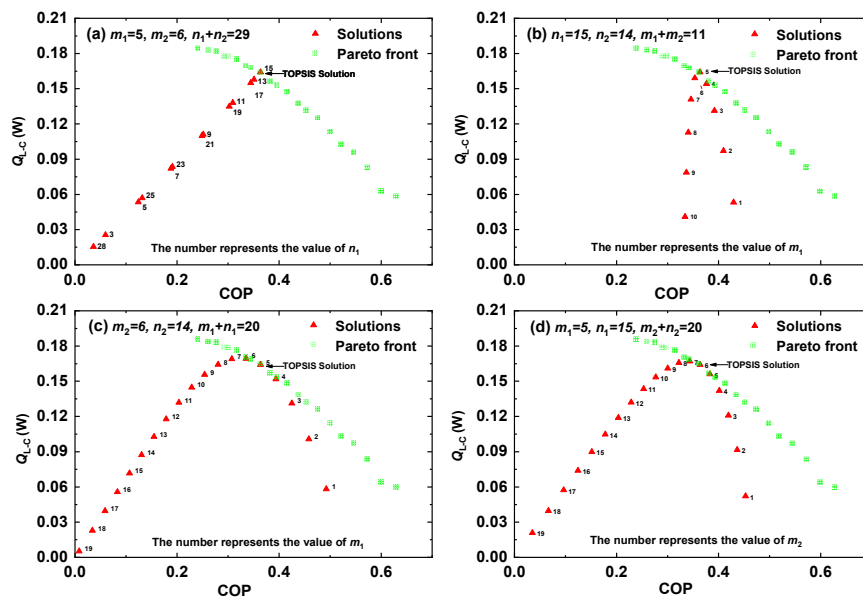

Figure 13. The effect of element number allocated to each stage on the performance of CTE under four different conditions: (**a**) different number ratio between the top and the lower stage of TEC when the element number allocated to TEG is fixed; (**b**) different number ratio between the top and the lower stage of TEG when the element number allocated to TEC is fixed; (**c**) different number ratio between the TEG module and the TEC module for the two top stages of CTE when the element number allocated to the two lower stages of CTE is fixed; and (**d**) different number ratio between the TEG module and the TEC module for the two lower stages of CTE when the element number allocated to the two top stages of CTE is fixed.
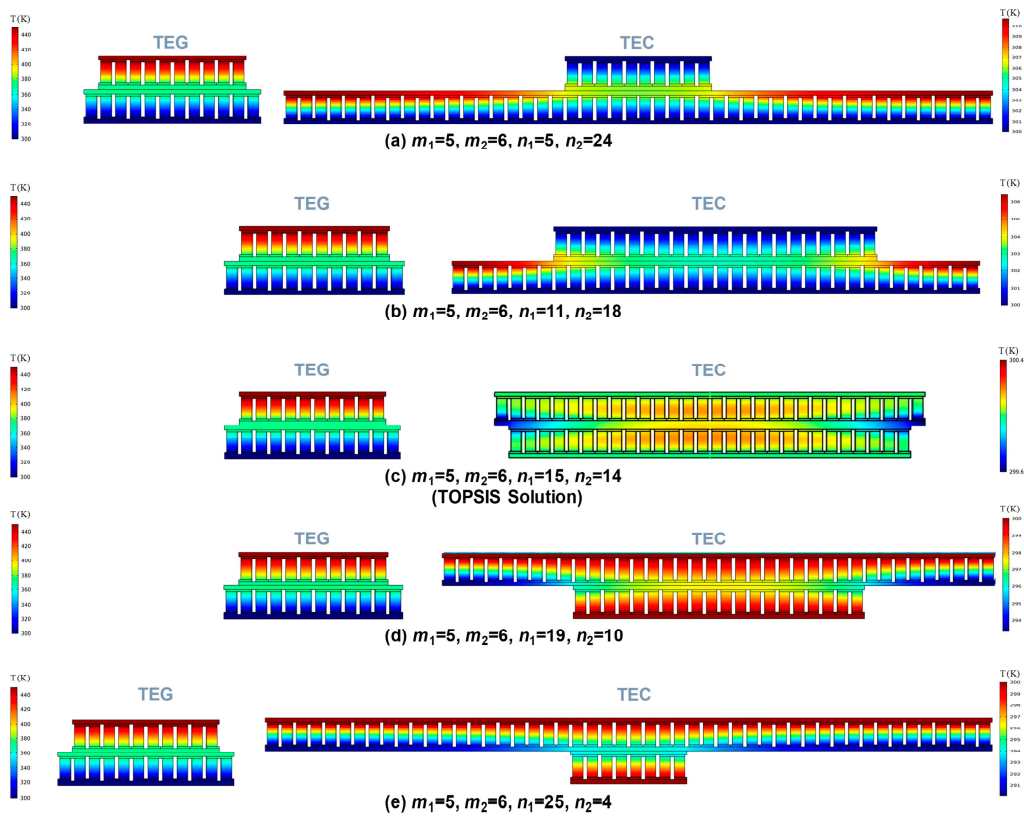
Figure 14. Temperature profiles of the structures with $n_1 = 5, 11, 15, 19$, and 25, corresponding the results shown in Figure 13a.
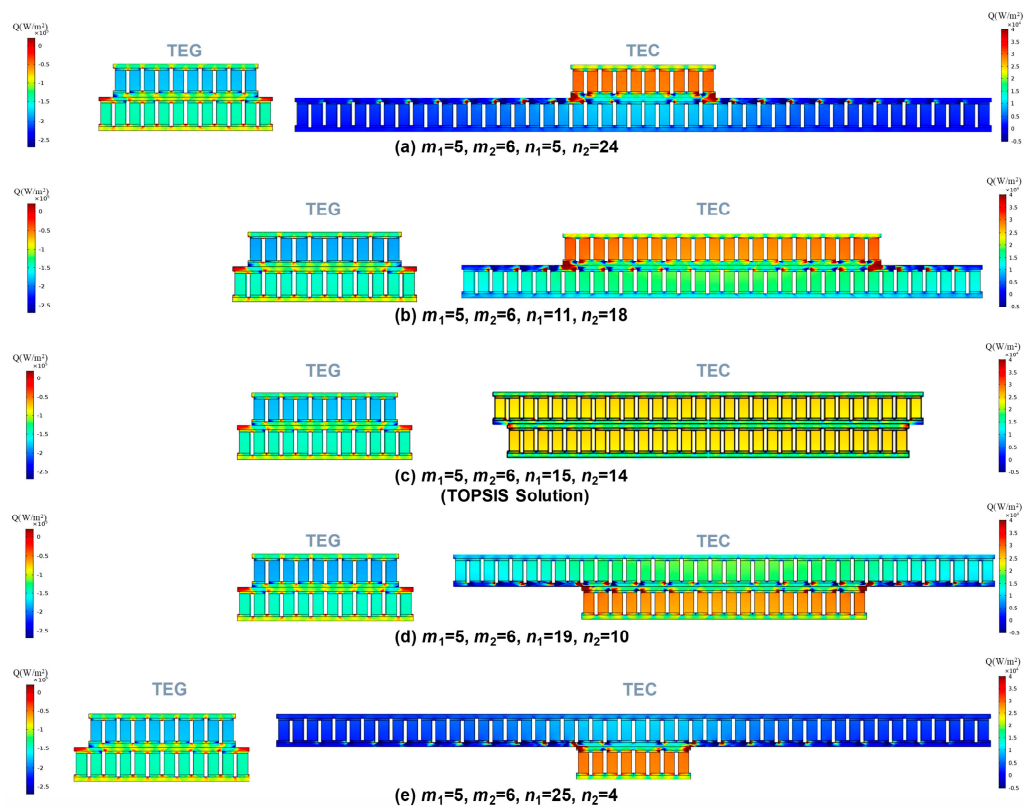

Figure 15. Heat flux distribution of the structures with $n_1 = 5, 11, 15, 19$, and 25, corresponding the results shown in Figure 13a.

5. Conclusions

In this paper, the effect of number allocation to each stage in a two-stage thermoelectric combined device is investigated by a three-dimensional multi-physics model. Multi-objective genetic algorithm NSGA-II as well as finite element method are coupled to solve this problem. After optimization, a set of Pareto-optimal solutions are obtained. Based on simultaneously considering Q_{L-C} and COP, the best compromised alternative solution is determined by the TOPSIS technique. The main conclusions can be summarized as follows: (1) An appropriate element number ratio between the TEG and TEC as well as between the two stages for TEG and TEC is significant for the combined thermoelectric device performance. The heat accumulated at the stage interfaces is responsible for the deteriorated performance. This issue can be alleviated and the performance can be improved by optimizing the element number allocated to each stage in the combined system. (2) Under the constraint of total element number of 40 for the CTE, the optimal element number for the top and the lower stage of the TEG module is 5 and 6, respectively; the optimal element number for the top and the lower stage of the TEC module is 15 and 14, respectively. After optimization, the cooling capacity is improved by 23.3% and COP is increased by 122.0% when compared with the 1# Initial Solution. (3) The heat transport equilibrium between the TEG module and the TEC module or between the top stage and the lower stage of the CTE is the key point to determine the device performance.

Author Contributions: conceptualization, J.-H.M. and H.-C.W.; methodology, J.-H.M. and H.-C.W.; software, H.-C.W.; validation, H.-C.W.; formal analysis, J.-H.M., H.-C.W. and T.-H.W.; investigation, H.-C.W.; resources, H.-C.W.; data curation, H.-C.W.; writing—original draft preparation, T.-H.W.; writing—review and editing, T.-H.W. and H.-C.W.; supervision, J.-H.M. and T.-H.W.; funding acquisition, J.-H.M. and T.-H.W.

Conflicts of Interest: The authors declare no conflict of interest.

Nomenclature

A	the cross-sectional area at the interface
f	objective function
I	electrical current flows through each element of the CTE (A)
$\vec{J}$	current density vector
k	thermal conductivity (W m^{-1} K^{-1})
m_1	the element number in the top stage of the TEG
m_2	the element number in the lower stage of the TEG
N	population size of optimization algorithm
n_1	the element number in the top stage of the TEC
n_2	the element number in the lower stage of the TEC
Q_{H-C}	heat that TEC dissipates to the heat sink at the hot end (W)
Q_{H-G}	heat that TEG absorbs from the heat source at the hot end (W)
Q_{L-C}	heat that TEC absorbs from the refrigerated object at the cold end (W)
Q_{L-G}	heat that TEG reject to the heat sink at the cold end (W)
T	absolute temperature (K)
T_{H-C}	temperature at the hot end of the top stage in TEC (K)
T_{H-G}	temperature at the hot end of the top stage in TEG (K)
T_{L-C}	temperature at the cold end of the lower stage in TEC (K)
T_{L-G}	temperature at the cold end of the lower stage in TEG (K)
ZT	figure of merit

Greek letters

α	Seebeck coefficient (V K^{-1})
β	Thomson coefficient (V K^{-1})
ρ	electric resistance (Ω m)
ψ	electric potential (V)

Acronyms and abbreviations

COP   coefficient of performance
CTE   combined thermoelectric device
NSGA-II   Non-dominated Sorting Genetic Algorithm II
TEC   thermoelectric cooler
TEG   thermoelectric generator
TOPSIS   Technique for Order Preference by Similarity to an Ideal Solution

Subscripts and Superscript

Ce   ceramic plate
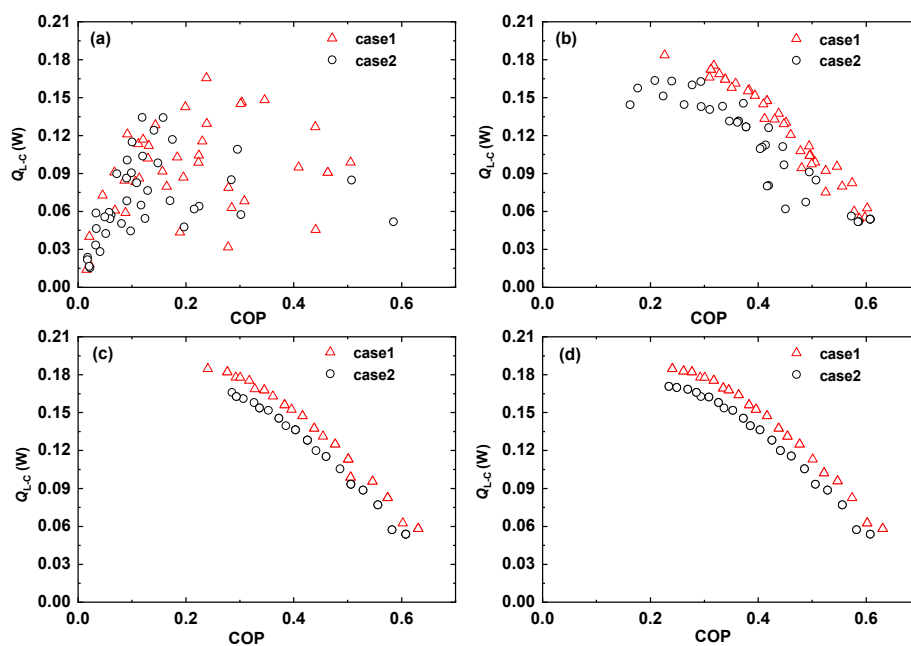Cu   copper connector
max   maximum

Appendix A

Figure A1. Comparison of distribution of Pareto fronts between case 1 and case 2: (**a**) the first generation; (**b**) the fourth generation; (**c**) the tenth generation; and (**d**) the eightieth generation. In case 1, k_{Ce} is determined by Equation (A1). In case 2, k_{Ce} is determined by Equation (A2).

$$k_{Ce} = 175 \, \text{W} \cdot \text{m}^{-1} \cdot \text{K}^{-1} \tag{A1}$$

$$k_{Ce} = \left(573,275 - 2037.1T + 3T^2 - 0.00156T^3 \right) \times 10^{-4} \, \text{W m}^{-1} \, \text{K}^{-1} \tag{A2}$$

Appendix B

Table A1. The value of search variables and performance metrics for the improved CTE system.

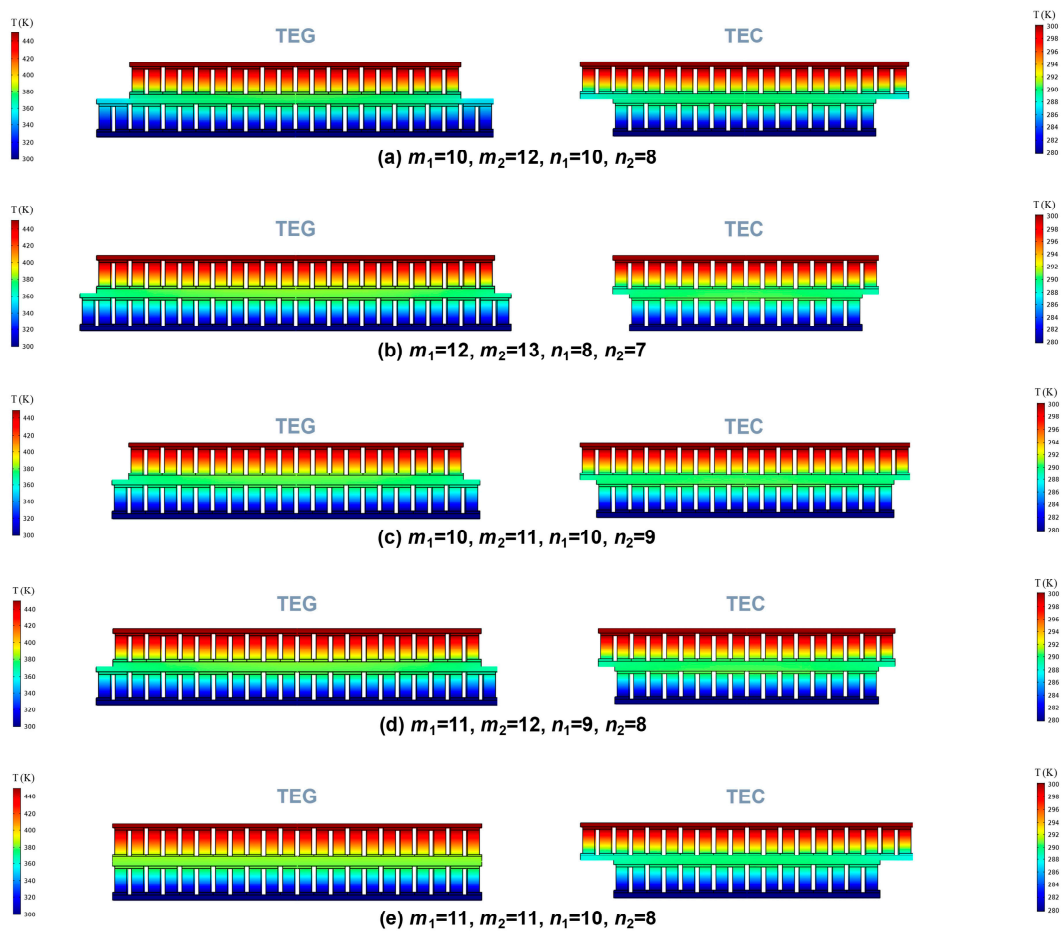| Individual Number	Allocation Design Parameters				Q_{L-C}(W)	COP
	m_1	m_2	n_1	n_2		
1	10	8	10	12	0.062	0.065
2	8	7	12	13	0.067	0.058
3	10	9	10	11	0.062	0.067
4	9	8	11	12	0.066	0.064
5	10	8	11	11	0.063	0.064

Figure A2. Temperature profiles of five different allocation design with: (**a**) $m_1 = 10$, $m_2 = 12$, $n_1 = 10$, $n_2 = 8$; (**b**) $m_1 = 12$, $m_2 = 13$, $n_1 = 8$, $n_2 = 7$; (**c**) $m_1 = 10$, $m_2 = 11$, $n_1 = 10$, $n_2 = 9$; (**d**) $m_1 = 11$, $m_2 = 12$, $n_1 = 9$, $n_2 = 8$; and (**e**) $m_1 = 11$, $m_2 = 11$, $n_1 = 10$, $n_2 = 8$.

Appendix C

Table A2. Numerical parameters of optimization algorithm.

Population Size	Generation	Pareto Fraction	Crossover Fraction	Migration Rate	Mutation Rate
40	80	0.7	0.8	0.2	0.01

Definitions in Table A1: Population size: a population is an array of individuals; Generation: maximum number of iterations before procedure termination; Pareto fraction: limiting the number of individuals on the Pareto front to keep the most fit population down to the specified fraction in order to maintain a diverse population; Crossover fraction: specifying the fraction of the population, other than elite children, that are crossover children; Migration rate: specifying how many individuals move between sub-populations; Mutation rate: controls the standard deviation of the mutation at the first generation, which is Scale multiplied by the range of the initial population.

Table A3. Structural parameters of optimization algorithm.

Structural Parameters	Option
Coding scheme	binary encoding
Selection	binary tournament
Crossover	arithmetic crossover
Mutation	Gaussian mutation
Constraint	constraint-dominate definition [46]
Stopping criterion	maximum iteration numbers

Table A4. The value of search variables and performance metrics for the improved CTE system.

Individual Number	Allocation Design Parameters				Q_{L-C}(W)	COP	I(A)
	m_1	m_2	n_1	n_2			
1	1	2	19	18	0.058	0.631	0.025
2	1	3	18	18	0.063	0.602	0.028
3	2	2	18	18	0.083	0.574	0.037
4	2	3	18	17	0.096	0.547	0.045
5	2	4	17	17	0.102	0.522	0.049
6	3	3	17	17	0.113	0.501	0.055
7	3	4	17	16	0.125	0.477	0.062
8	3	5	16	16	0.131	0.454	0.068
9	4	4	16	16	0.138	0.438	0.071
10	4	5	16	15	0.147	0.416	0.079
11	4	6	15	15	0.153	0.396	0.085
12	5	5	15	15	0.156	0.383	0.087
13 [1]	5	6	15	14	0.164	0.364	0.096
14	5	7	14	14	0.168	0.345	0.102
15	6	6	14	14	0.169	0.335	0.103
16	6	7	14	13	0.175	0.318	0.111
17	6	8	13	13	0.178	0.301	0.117
18	7	7	13	13	0.178	0.293	0.117
19	7	8	13	12	0.182	0.277	0.126
20	7	9	12	12	0.183	0.261	0.132
21	8	9	12	11	0.185	0.241	0.140

[1] The TOPSIS selected individual.

References

1. Bell, L.E. Cooling, heating, generating power, and recovering waste heat with thermoelectric systems. *Science* **2008**, *321*, 1457–1461. [CrossRef] [PubMed]
2. He, W.; Zhang, G.; Zhang, X.; Ji, J.; Li, G.; Zhao, X. Recent development and application of thermoelectric generator and cooler. *Appl. Energy* **2015**, *143*, 1–25. [CrossRef]
3. Sun, D.; Liu, G.; Shen, L.; Chen, H.; Yao, Y.; Jin, S. Modeling of high power light-emitting diode package integrated with micro-thermoelectric cooler under various interfacial and size effects. *Energy Convers. Manag.* **2019**, *179*, 81–90. [CrossRef]
4. Zhang, H.; Kong, W.; Dong, F.; Xu, H.; Chen, B.; Ni, M. Application of cascading thermoelectric generator and cooler for waste heat recovery from solid oxide fuel cells. *Energy Convers. Manag.* **2017**, *148*, 1382–1390. [CrossRef]
5. Kwan, T.H.; Wu, X.; Yao, Q. Multi-objective genetic optimization of the thermoelectric system for thermal management of proton exchange membrane fuel cells. *Appl. Energy* **2018**, *217*, 314–327. [CrossRef]
6. Babu, C.; Ponnambalam, P. The role of thermoelectric generators in the hybrid PV/T systems: A review. *Energy Convers. Manag.* **2017**, *151*, 368–385. [CrossRef]
7. Stathopoulos, P.; Fernàndez-Villa, J. On the potential of power generation from thermoelectric generators in gas turbine combustors. *Energies* **2018**, *11*, 2769. [CrossRef]
8. Zhang, G.; Fan, L.; Niu, Z.; Jiao, K.; Diao, H.; Du, Q.; Shu, G. A comprehensive design method for segmented thermoelectric generator. *Energy Convers. Manag.* **2015**, *106*, 510–519. [CrossRef]
9. Wang, X.D.; Huang, Y.X.; Cheng, C.H.; Lin, D.T.W.; Kang, C.H. A three-dimensional numerical modeling of thermoelectric device with consideration of coupling of temperature field and electric potential field. *Energy* **2012**, *47*, 488–497. [CrossRef]
10. Zhao, D.; Tan, G. A review of thermoelectric cooling: Materials, modeling and applications. *Appl. Therm. Eng.* **2014**, *66*, 15–24. [CrossRef]
11. Chen, W.H.; Wang, C.C.; Hung, C.I. Geometric effect on cooling power and performance of an integrated thermoelectric generation-cooling system. *Energy Convers. Manag.* **2014**, *87*, 566–575. [CrossRef]

12.　Wang, T.H.; Wang, Q.H.; Leng, C.; Wang, X.D. Parameter analysis and optimal design for two-stage thermoelectric cooler. *Appl. Energy* **2015**, *154*, 1–12. [CrossRef]

13.　Ge, Y.; Liu, Z.; Sun, H.; Liu, W. Optimal design of a segmented thermoelectric generator based on three-dimensional numerical simulation and multi-objective genetic algorithm. *Energy* **2018**, *147*, 1060–1069. [CrossRef]

14.　Sun, H.; Ge, Y.; Liu, W.; Liu, Z. Geometric optimization of two-stage thermoelectric generator using genetic algorithms and thermodynamic analysis. *Energy* **2019**, *171*, 37–48. [CrossRef]

15.　Sun, H.; Gil, S.U.; Liu, W.; Liu, Z. Structure optimization and exergy analysis of a two-stage TEC with two different connections. *Energy* **2019**, *180*, 175–191. [CrossRef]

16.　Chen, J.; Li, K.; Liu, C.; Li, M.; Lv, Y.; Jia, L.; Jiang, S. Enhanced efficiency of thermoelectric generator by optimizing mechanical and electrical structures. *Energies* **2017**, *10*, 1329. [CrossRef]

17.　Liang, Y.; Ge, M.; Liang, Z.; Wang, S.; Zhao, Y.; Li, Y. Performance analysis of automobile exhaust thermoelectric generator system with media fluid. *Energy Convers. Manag.* **2018**, *171*, 427–437.

18.　Yu, C.; Yang, S.H.; Pak, S.Y.; Youn, J.R.; Song, Y.S. Graphene embedded form stable phase change materials for drawing the thermo-electric energy harvesting. *Energy Convers. Manag.* **2018**, *169*, 88–96. [CrossRef]

19.　Daghigh, R.; Khaledian, Y. Effective design, theoretical and experimental assessment of a solar thermoelectric cooling-heating system. *Sol. Energy* **2018**, *162*, 561–572. [CrossRef]

20.　Ebrahimi, M.; Derakhshan, E. Design and evaluation of a micro combined cooling, heating, and power system based on polymer exchange membrane fuel cell and thermoelectric cooler. *Energy Convers. Manag.* **2018**, *171*, 507–517. [CrossRef]

21.　Rattner, A.S.; Meehan, T.J. Simple analytic model for optimally sizing thermoelectric generator module arrays for waste heat recovery. *Appl. Therm. Eng.* **2019**, *146*, 795–804. [CrossRef]

22.　Comamala, M.; Cózar, I.R.; Massaguer, A.; Massaguer, E.; Pujol, T. Effects of design parameters on fuel economy and output power in an automotive thermoelectric generator. *Energies* **2018**, *11*, 3274. [CrossRef]

23.　Zhang, C.W.; Xu, K.J.; Li, L.Y.; Yang, M.Z.; Gao, H.B.; Chen, S.R. Study on a battery thermal management system based on a thermoelectric effect. *Energies* **2018**, *11*, 279. [CrossRef]

24.　von Lukowicz, M.; Abbe, E.; Schmiel, T.; Tajmar, M. Thermoelectric generators on satellites—An approach for waste heat recovery in space. *Energies* **2016**, *9*, 541. [CrossRef]

25.　Cheng, K.; Feng, Y.; Lv, C.; Zhang, S.; Qin, J.; Bao, W. Performance evaluation of waste heat recovery systems based on semiconductor thermoelectric generators for hypersonic vehicles. *Energies* **2017**, *10*, 570. [CrossRef]

26.　Ritz, F.; Peterson, C.E. Multi-mission radioisotope thermoelectric generator (MMRTG) program overview. In Proceedings of the 2004 IEEE Aerospace Conference Proceedings (IEEE Cat. No. 04TH8720), Big Sky, MT, USA, 6–13 March 2004; Volume 5, pp. 2950–2957.

27.　Atta, R.M. Solar water condensation using thermoelectric coolers. *Int. J. Adv. Eng. Res. Dev.* **2018**, *4*, 142–145.

28.　Karami Rad, M.; Omid, M.; Rajabipour, A.; Tajabadi, F.; Aistrup Rosendahl, L.; Rezaniakolaei, A. Optimum thermal concentration of solar thermoelectric generators (STEG) in realistic meteorological condition. *Energies* **2018**, *11*, 2425. [CrossRef]

29.　Eisenhut, C.; Bitschi, A. Thermoelectric conversion system based on geothermal and solar heat. In Proceedings of the 2006 25th International Conference on Thermoelectrics, Vienna, Austria, 6–10 August 2006; pp. 510–515.

30.　Khattab, N.M.; El Shenawy, E.T. Optimal operation of thermoelectric cooler driven by solar thermoelectric generator. *Energy Convers. Manag.* **2006**, *47*, 407–426. [CrossRef]

31.　Chen, X.; Lin, B.; Chen, J. The parametric optimum design of a new combined system of semiconductor thermoelectric devices. *Appl. Energy* **2006**, *83*, 681–686. [CrossRef]

32.　Meng, F.; Chen, L.; Sun, F. Performance optimization for two-stage thermoelectric refrigerator system driven by two-stage thermoelectric generator. *Cryogenics* **2009**, *49*, 57–65. [CrossRef]

33.　Meng, F.; Chen, L.; Sun, F. Multiobjective analyses of physical dimension on the performance of a TEG-TEC system. *Int. J. Low-Carbon Technol.* **2010**, *5*, 193–200. [CrossRef]

34.　Meng, F.; Chen, L.; Sun, F. Performance analysis for two-stage TEC system driven by two-stage TEG obeying Newton's heat transfer law. *Math. Comput. Model.* **2010**, *52*, 586–595. [CrossRef]

35.　Chen, L.; Meng, F.; Sun, F. Effect of heat transfer on the performance of thermoelectric generator-driven thermoelectric refrigerator system. *Cryogenics* **2012**, *52*, 58–65. [CrossRef]

36. Chen, L.; Meng, F.; Ge, Y.; Sun, F. Optimum variables selection of thermoelectric generator-driven thermoelectric refrigerator at different source temperature. *Int. J. Ambient Energy* **2012**, *33*, 108–117. [CrossRef]

37. Meng, F.; Chen, L.; Sun, F. Effects of thermocouples' physical size on the performance of the TEG-TEH system. *Int. J. Low-Carbon Technol.* **2016**, *11*, 37–382. [CrossRef]

38. Feng, Y.; Chen, L.; Meng, F.; Sun, F. Influences of external heat transfer and Thomson effect on the performance of TEG-TEC combined thermoelectric device. *Sci. China Technol. Sci.* **2018**, *61*, 1600–1610. [CrossRef]

39. Teffah, K.; Zhang, Y.; Mou, X.L. Modeling and experimentation of new thermoelectric cooler-thermoelectric generator module. *Energies* **2018**, *11*, 576. [CrossRef]

40. Kwan, T.H.; Wu, X.; Yao, Q. Integrated TEG-TEC and variable coolant flow rate controller for temperature control and energy harvesting. *Energy* **2018**, *159*, 448–456. [CrossRef]

41. Kwan, T.H.; Wu, X.; Yao, Q. Thermoelectric device multi-objective optimization using a simultaneous TEG and TEC characterization. *Energy Convers. Manag.* **2018**, *168*, 85–97. [CrossRef]

42. Feng, Y.; Chen, L.; Meng, F.; Sun, F. Influences of the Thomson effect on the performance of a thermoelectric generator-driven thermoelectric heat pump combined device. *Entropy* **2018**, *20*, 29. [CrossRef]

43. Yoo, C.Y.; Yeon, C.; Jin, Y.; Kim, Y.; Song, J.; Yoon, H.; Park, S.H.; Beltrán-Pitarch, B.; García-Cañadas, J.; Min, G. Determination of the thermoelectric properties of a skutterudite-based device at practical operating temperatures by impedance spectroscopy. *Appl. Energy* **2019**, *251*, 113341. [CrossRef]

44. Meng, J.H.; Zhang, X.X.; Wang, X.D. Multi-objective and multi-parameter optimization of a thermoelectric generator module. *Energy* **2014**, *71*, 367–376. [CrossRef]

45. Meng, J.H.; Zhang, X.X.; Wang, X.D. Characteristics analysis and parametric study of a thermoelectric generator by considering variable material properties and heat losses. *Int. J. Heat Mass Transf.* **2015**, *80*, 227–235. [CrossRef]

46. Deb, K.; Member, A.; Pratap, A.; Agarwal, S.; Meyarivan, T. A fast and elitist multiobjective genetic algorithm: NSGA-II. *IEEE Trans. Evol. Comput.* **2002**, *6*, 182–197. [CrossRef]

47. Lai, Y.J.; Liu, T.Y.; Hwang, C.L. Topsis for MODM. *Eur. J. Oper. Res.* **1994**, *76*, 486–500. [CrossRef]

48. Deb, K. Multi-Objective Optimization. In *Search Methodologies*; Springer: Boston, MA, USA, 2014; pp. 403–449.

49. Hu, X.; Yamamoto, A.; Ohta, M.; Nishiate, H. Measurement and simulation of thermoelectric efficiency for single leg. *Rev. Sci. Instrum.* **2015**, *86*, 45103. [CrossRef]

50. Xuan, X.C.; Ng, K.C.; Yap, C.; Chua, H.T. Optimization of two-stage thermoelectric coolers with two design configurations. *Energy Convers. Manag.* **2002**, *43*, 2041–2052. [CrossRef]

51. Wang, X.D.; Wang, Q.H.; Xu, J.L. Performance analysis of two-stage TECs (thermoelectric coolers) using a three-dimensional heat-electricity coupled model. *Energy* **2014**, *65*, 419–429. [CrossRef]